PNAS
www.pnas.org

Supplementary Information for

Earth's radiative imbalance from the Last Glacial Maximum to the present

Daniel Baggenstos, Marcel Häberli, Jochen Schmitt, Sarah A. Shackleton, Benjamin Birner, Jeffrey P. Severinghaus, Thomas Kellerhals and Hubertus Fischer

Corresponding author: Daniel Baggenstos.
E-mail: baggenstos@climate.unibe.ch

This PDF file includes:

Supporting Information Text

Estimation of LGM-Holocene changes in the heat content of various climate components

This section presents estimates of glacial/interglacial changes in the energy content of climate sub-systems other than the ocean and continental ice masses. The following paragraphs detail the calculations, whereas the results are summarized in Table S1. OHC and LHM clearly dominate the deglacial changes in energy content, with all other components being at least one order of magnitude smaller.

Dry atmosphere. The mass of the dry atmosphere is $5.1 * 10^{18}$ kg (1). The specific heat capacity of dry air is 1.0 kJ kg^{-1} K^{-1}, with a small dependence on temperature, which is negligible for our purposes. Assuming a mean atmospheric temperature change of 4 K from the LGM to the Holocene (2), the heat content of the dry atmosphere has increased by $2.0 * 10^{22}$ J over the same period, i.e., three orders of magnitude smaller than OHC and LHM.

Atmospheric water vapor. The mean mass of water vapor in the atmosphere is $1.3 * 10^{16}$ kg (1). The latent heat of vaporization for water is roughly 2,500 kJ kg^{-1} with a small but for our purposes negligible temperature dependence. Assuming a doubling of atmospheric water vapor from the LGM to the Holocene (a conservative estimate, as modeled LGM water vapor content is only ∼30% lower than today (3)), the latent heat of water in the atmosphere has increased by $3.1 * 10^{22}$ J, i.e., three orders of magnitude smaller than OHC and LHM.

Sea ice. Perennial sea ice in the Arctic during the Holocene was likely covering a larger area than during the LGM because lowered sea level reduces the area of the polar oceans (4). In the Southern Hemisphere, summer sea ice extent is poorly constrained by data. Proxies and models agree on a approximate doubling of area coverage of winter sea ice for the LGM, equivalent to an increase in sea ice area by $2 * 10^7$ km^2. Assuming that perennial SH sea ice increased by the same amount and an average sea ice thickness of 5 m (4), the energy required to melt $\sim 4.1 * 10^{16}$ kg of sea ice is $1.4 * 10^{22}$ J, i.e., three orders of magnitude smaller than OHC and LHM.

Subsurface. Continental heat storage has increased by $\sim 1.0 * 10^{22}$ J in the 2nd half of the 20th century (5, 6), and is thus a non-negligible contributor to the current heat budget. To our knowledge, there are no assessments of glacial/interglacial changes in continental heat storage in the literature. As a first order estimate we calculate the excess heat stored in an infinitely large subsurface layer in response to a sinusoidal surface temperature variation with amplitude ΔT of 1.5 K and a period P of 20,000 years, by solving the Fourier heat equation subject to the surface boundary condition as described e.g. by (7). In this idealized problem the e-folding depth of the sinusoid is described as $z^* = \sqrt{\frac{KP}{\pi}}$ with K the ground's thermal diffusivity and P the period of the sine wave. Subsurface thermal diffusivity is highly variable from 0.1 to 2.7 $\times$ 10^{-6} m^2 s^{-1} depending on rock type (8). Using a typical thermal diffusivity for carbonate rock of 1.2 $\times$ 10^{-6} m^2 s^{-1} yields a z^* of 491 m. Integrating the temperature variation from the surface to 10 times the e-folding depth and multiplying the average temperature signal with a typical crustal density of 2750 kg m^{-3} and a specific heat capacity of 800 J kg^{-1} K^{-1} gives 162 MJ m^{-2} of heat stored in the subsurface. Multiplying this times the surface of Earth (thus including continental and oceanic crust) produces our final estimate of glacial/interglacial change in near-surface heat storage of $8.3 * 10^{23}$ J, i.e., more than one order of

magnitude smaller than OHC and LHM. This estimate is likely too high as bottom waters in the ocean are already close to the freezing point and thus cannot cool by 3 K.

Groundwater. There is $22 * 10^6$ km^3 of groundwater in the uppermost 2 km of Earth's crust (9). It is difficult to assess what fraction of this can be affected by glacial/interglacial temperature variations because global recharge rates are poorly known. Modelled global recharge rates in the late 20th century are on the order of 15,000 km^3 a^{-1} (10). This would suffice to replace the entire groundwater volume in ~1,500 years, but it is also known that recharge rates vary greatly (11) and some groundwater has been reported to be older than 2 million years (12). To get an extreme upper limit estimate, we assume that the entire global groundwater volume warmed by 3 K from the LGM to the Holocene, thus taking up $2.6 * 10^{23}$ J of energy. Even under this unrealistic assumption, the groundwater contribution to the planetary energy budget is still almost two orders of magnitude smaller than that of OHC and LHM.

Chemical energy stored in the photosynthesis products of the biosphere. Photosynthesis requires ~477 kJ of energy to produce 1 mol (12 g) of carbon in the form of glucose (13). The glacial-interglacial difference in land biosphere carbon inventory is poorly known with estimates ranging from -400 to +1,500 GtC (14). Assuming a 600 GtC increase in the terrestrial biosphere, the photosynthetic energy stored in it increased by $2.4 * 10^{19}$ J, i.e., six orders of magnitude less than OHC and LHM.

Heavy isotope deficit

In this section we explore the effect of including a correction for differential kinetic isotope fractionation on our results.

Firn air processes. Isotopic enrichment in the firn column is thought to be affected by diffusion, advection, dispersion, and convective mixing (15, 16). Molecular diffusion drives the isotopic enrichment towards gravitational and thermal equilibrium while advection, dispersion, and convection act to erase the enrichment. Heavier (more slowly diffusing) gases such as krypton and xenon will be further from equilibrium than lighter (faster diffusing) gases like nitrogen and argon, causing an apparent deficit in isotopic enrichment in the heavier gases compared to the lighter ones (16–18).

EDC data. Our isotopic data clearly show such a Heavy Isotope Deficit (HID) with krypton and xenon isotopes being less enriched than argon isotopes by on average 33 per meg and 48 per meg, respectively (Figure S3, all values normalized to unit mass difference). Similar HIDs have already been reported in ice core noble gas data from WD (19) and Taylor Glacier (20), but were not further explored for their effect on reconstructed MOTs. Although firn modeling efforts have not been able to quantitatively explain this amount of differential kinetic fractionation (17) the relative amount of fractionation between different gases (hereafter called the scaling) appears to be robust and unchanging in a variety of firn regimes. Using the scaling factors from (17), we can determine the amount of kinetic fractionation from our isotopic data and then apply it to the elemental ratios δKr/N$_2$, δXe/N$_2$ and δXe/Kr. To this end we solve the following equation with a least squares approach:

$$\begin{bmatrix} 7.33 - 1 \\ 5.25 - 1 \end{bmatrix} \times HID_{Ar} = \begin{bmatrix} Ar^* - Xe^* \\ Ar^* - Kr^* \end{bmatrix} \quad [1]$$

Ar^*, Kr^*, and Xe^* denote the unit mass normalized isotopic enrichments $\delta^{40/36}Ar/4$, $\delta^{86/84}Kr/2$, and the mean of $\delta^{136/129}Xe/7$, $\delta^{134/129}Xe/5$, and $\delta^{132/129}Xe/3$ weighted by the inverse of the instrumental precision, while HID_{Ar} is equivalent to ϵ'_{Ar} in (17)'s Figure 12. 7.33 is the ratio of ϵ'_{Xe} to ϵ'_{Ar} and 5.25 is the same for ϵ'_{Kr} to ϵ'_{Ar} from firn modeling. The fit of the scaling to the argon-krypton and argon-xenon isotopic differences is shown in Figure S4. The scaling factors from the firn model are able to match our isotopic data nicely. The scaling also predicts a small difference between argon and nitrogen isotopic values, which we do not clearly observe in our data (Figure S3). It is possible that a small offset is masked by the measurement noise, which is considerable especially for nitrogen isotopes that were measured with inferior precision (7 per meg per mass unit) compared to the noble gas isotopes (5 per meg per mass unit). Another possibility is that the argon isotopes are artifactually enriched due to mass-fractionating gas loss during storage.

Applying the empirically determined HID scaling to the elemental ratios decreases the LGM-Holocene MOT difference in the EDC record from 3.6 K to 2.7 K. This value now agrees well with the LGM-Holocene MOT difference from WD of 2.6 K (Figure S6). Furthermore, the scaling also reduces the difference between individual reconstructions from $\delta Kr/N_2$, $\delta Xe/N_2$ and $\delta Xe/Kr$ (Figure S5), which suggests that the correction is physically appropriate.

Applying the empirically determined scaling to the elemental ratios also enriches $\delta Kr/N_2$, $\delta Xe/N_2$ and $\delta Xe/Kr$ by on average 1.3 per mil, 4.3 per mil, and 2.9 per mil, respectively. This leads to MOT anomalies during the Holocene of approximately +2° C, which are unrealistically warm (Figure S5). Clearly, we are currently not able to capture all the physical processes affecting gas composition in ice cores at the per meg level. One such process that could at least qualitatively explain the enriched MOTs in the Holocene is enhanced winter convection due to a thermally unstable winter air column in the top few meters of the firn. In this case the fractionation due to seasonally changing surface temperature wouldn't cancel, causing a rectification of the thermal signal (21), which biases MOT to warmer temperatures. The ability of this hypothesized process to affect the firn isotopic ratios will be further explored in models and observations.

Significance for radiative imbalance results. Figure S6 shows the reconstructed deglacial energy changes, just as in Figure 1 but with the HID correction. Figure S7 shows the reconstructed planetary radiative imbalance, again with the HID correction. The shape of the OHC record is not substantially affected by the inclusion of the HID correction, and thus PRI still exhibits the two peaks. PRI is overall slightly reduced by about 15% as the glacial/interglacial OHC change is smaller but relative changes are not affected and the entire discussion based on our reconstruction is still valid.

Table S1. Summary of LGM-Holocene heat content estimates.

Reservoir	Type of assessment	Energy (J)
OHC		$1.4 - 1.9 \times 10^{25}$
LHM		1.8×10^{25}
Dry atmosphere	best estimate	2.0×10^{22}
Atmospheric H_2O	best estimate	3.1×10^{22}
Sea ice	upper limit	1.4×10^{22}
Subsurface	upper limit	8.3×10^{23}
Groundwater	extreme upper limit	2.6×10^{23}
Biosphere	best estimate	2.4×10^{19}

Table S2. Long term measurement reproducibility (given as the standard deviation of 28 measurements of 'ambient air' over 10 months).

Isotope ratio	Error (1-σ, per mil)	Instrument
δ^{15}N	0.007	Thermo DeltaV
$\delta^{40/36}$Ar	0.010	Thermo MAT253
$\delta^{86/84}$Kr	0.012	Thermo MAT253
$\delta^{86/82}$Kr	0.021	Thermo MAT253
$\delta^{132/129}$Xe	0.017	Thermo MAT253
$\delta^{136/129}$Xe	0.036	Thermo MAT253
δ^{84}Kr/^{40}Ar	0.088	Thermo MAT253
δ^{129}Xe/^{40}Ar	0.178	Thermo MAT253
δ^{132}Xe/^{40}Ar	0.203	Thermo MAT253
δ^{129}Xe/^{84}Kr	0.120	Thermo MAT253
δ^{132}Xe/^{84}Kr	0.135	Thermo MAT253
δ^{40}Ar/^{28}N$_2$	0.060	Thermo DeltaV

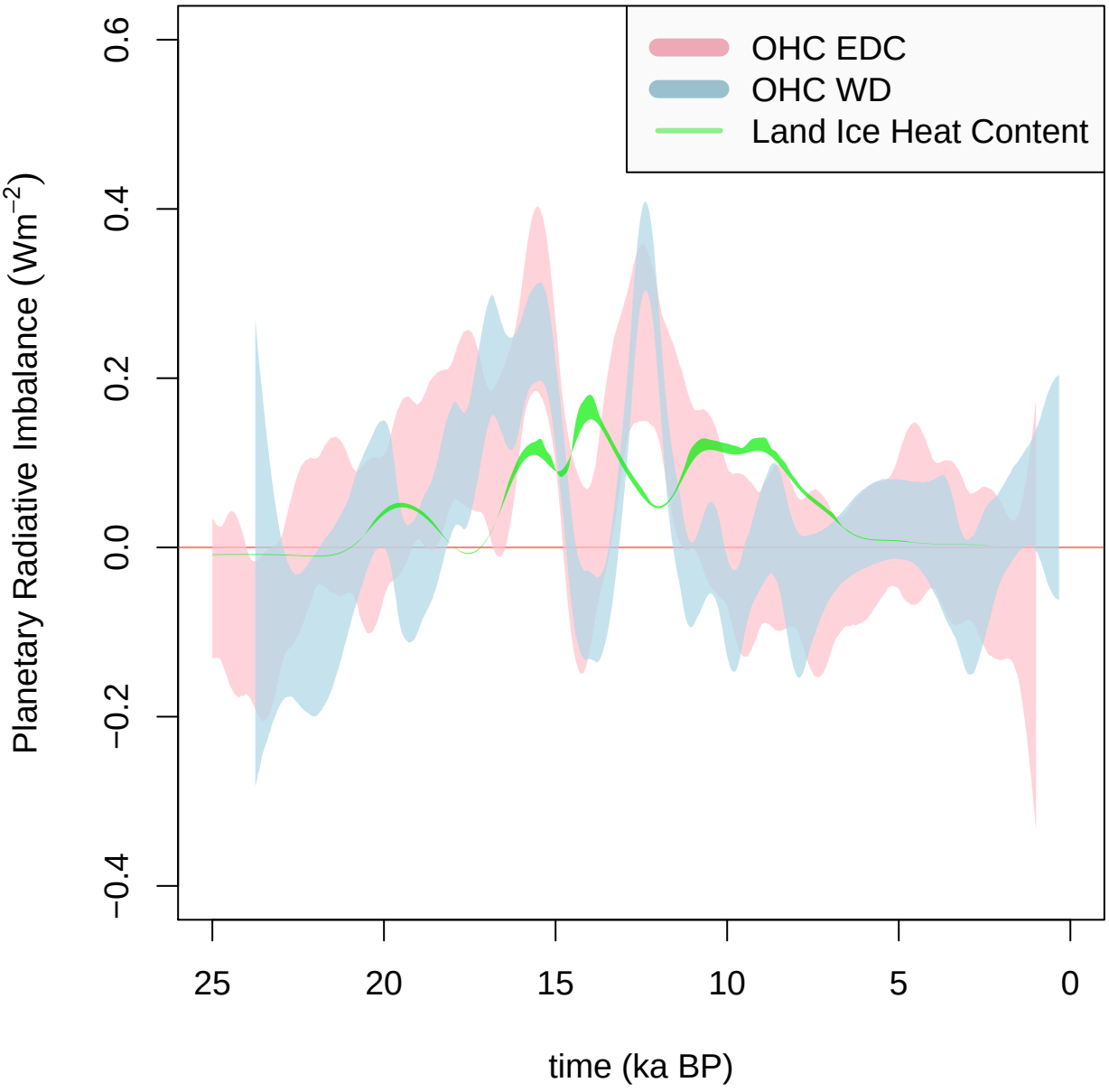

Fig. S1. Reconstructed individual contributions to PRI from OHC EDC (pink), OHC WAIS Divide (blue), and LHM (green) with 1-σ confidence band. The two peaks during the deglaciation are clearly associated with OHC changes, whereas the LHM contribution is less variable throughout the entire period.

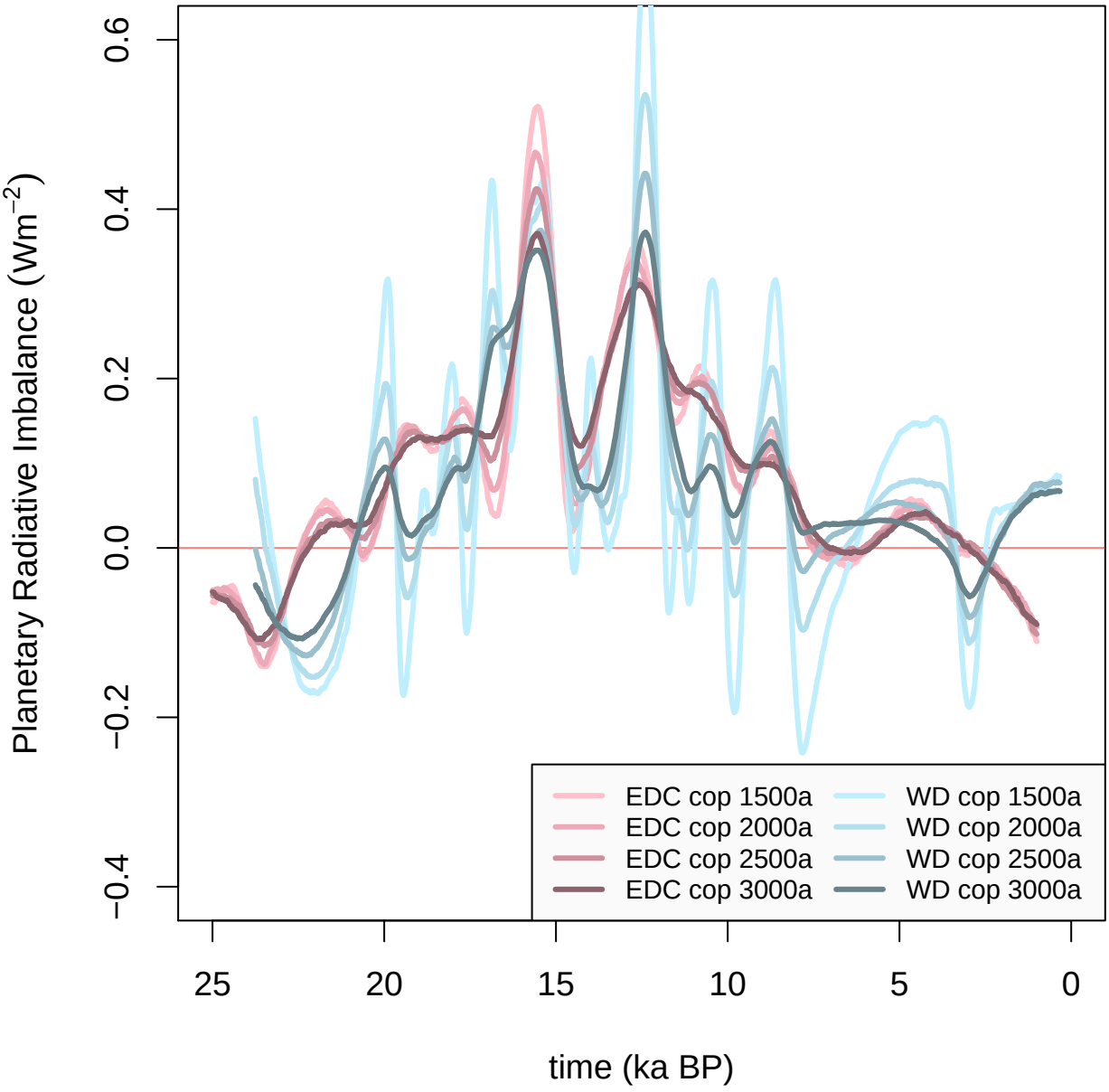

Fig. S2. Experiment to show the sensitivity of the reconstructed PRI with regards to the cut-off period in the smoothing spline. In pink, the EDC derived radiative imbalance with 4 different cut-off periods is shown. In blue, the same for WAIS Divide. With cut-off periods less than 2,000 years, the noise in the OHC records starts to dominate the signal. For very large cut-off periods (>3000 years) the smoothing starts to reduce the amplitude of the peaks significantly.

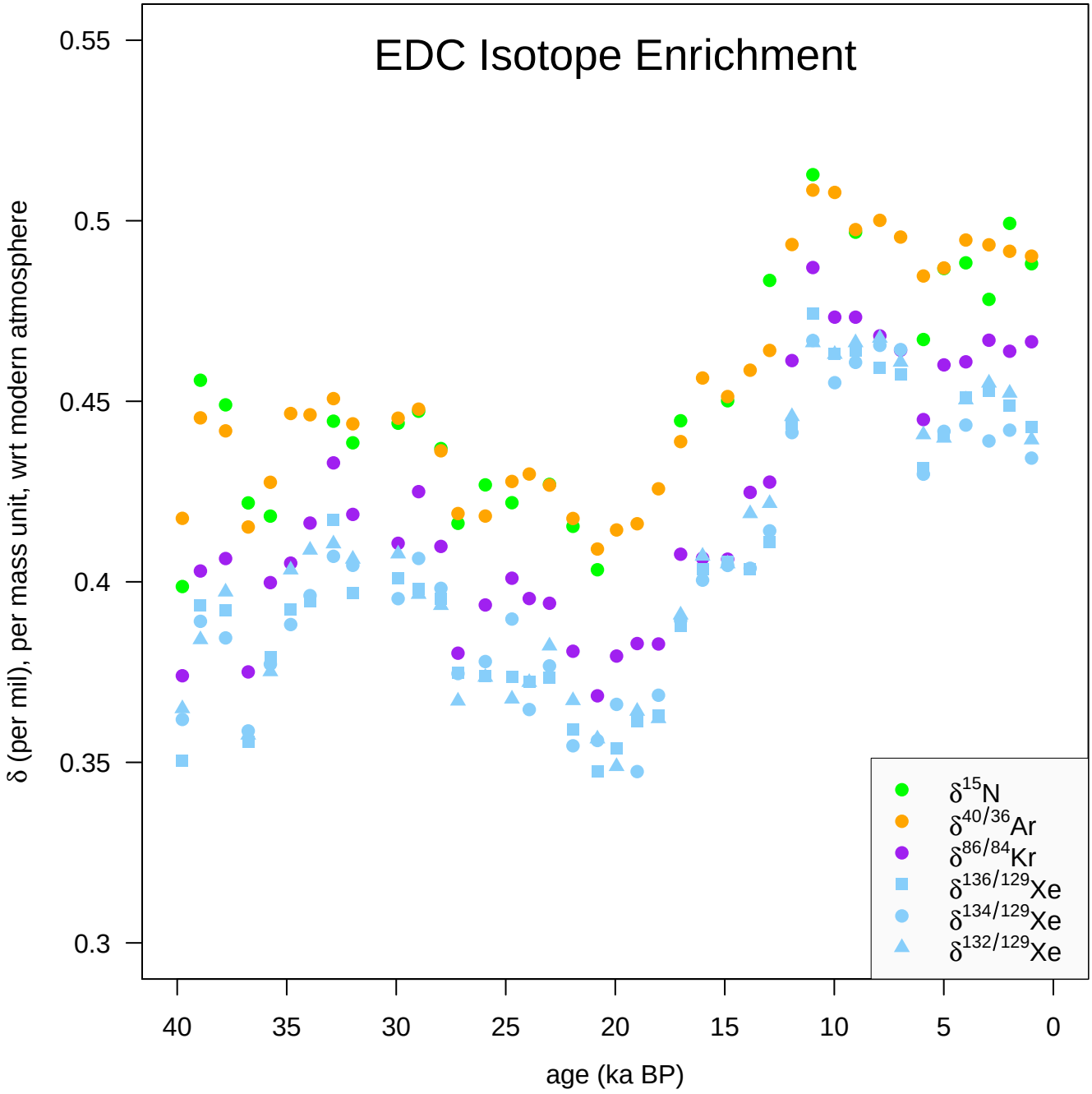

Fig. S3. Inert gas isotope enrichment in the EDC ice core from 40 ka to present-day. All data is reported relative to modern air sampled in Bern, Switzerland. The data is corrected for thermal fractionation as described in the Methods section. 12 δ^{15}N data points are not shown due to drilling fluid contamination causing isobaric interference on mass 29 and 82.

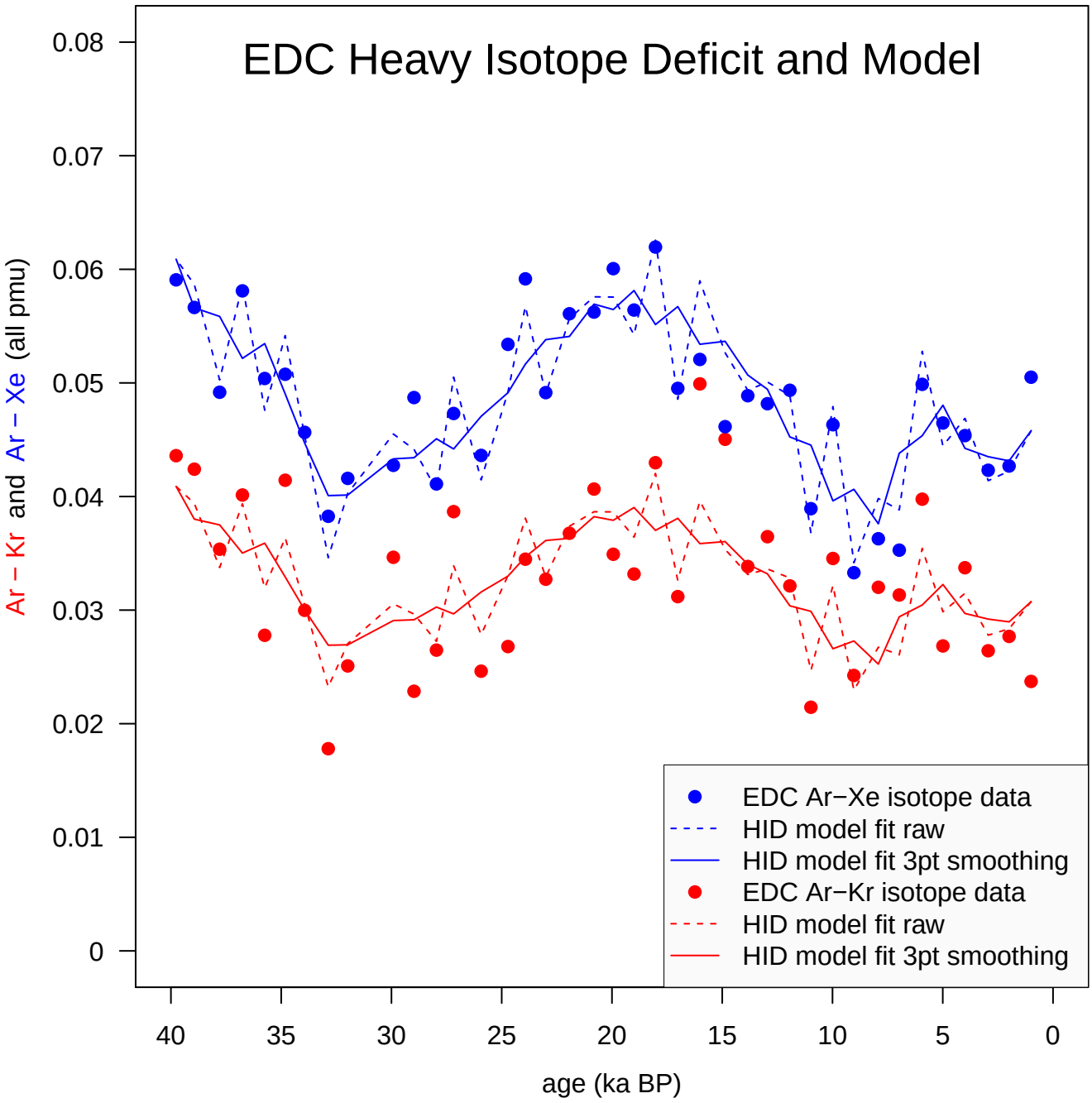

Fig. S4. HID for the EDC ice core exhibited by the argon-krypton and argon-xenon isotopic differences for the past 40,000 years. Lines show the model fit assuming differential kinetic isotope fractionation is causing the HID. The model achieves a good fit to both Ar^{*}-Kr^{*} and Ar^{*}-Xe^{*} using one free parameter (HID_{Ar} in equation S1). All isotopic data is reported as per mass unit.

Daniel Baggenstos, Marcel Häberli, Jochen Schmitt, Sarah A. Shackleton, Benjamin Birner, Jeffrey P. Severinghaus, Thomas Kellerhals and Hubertus Fischer

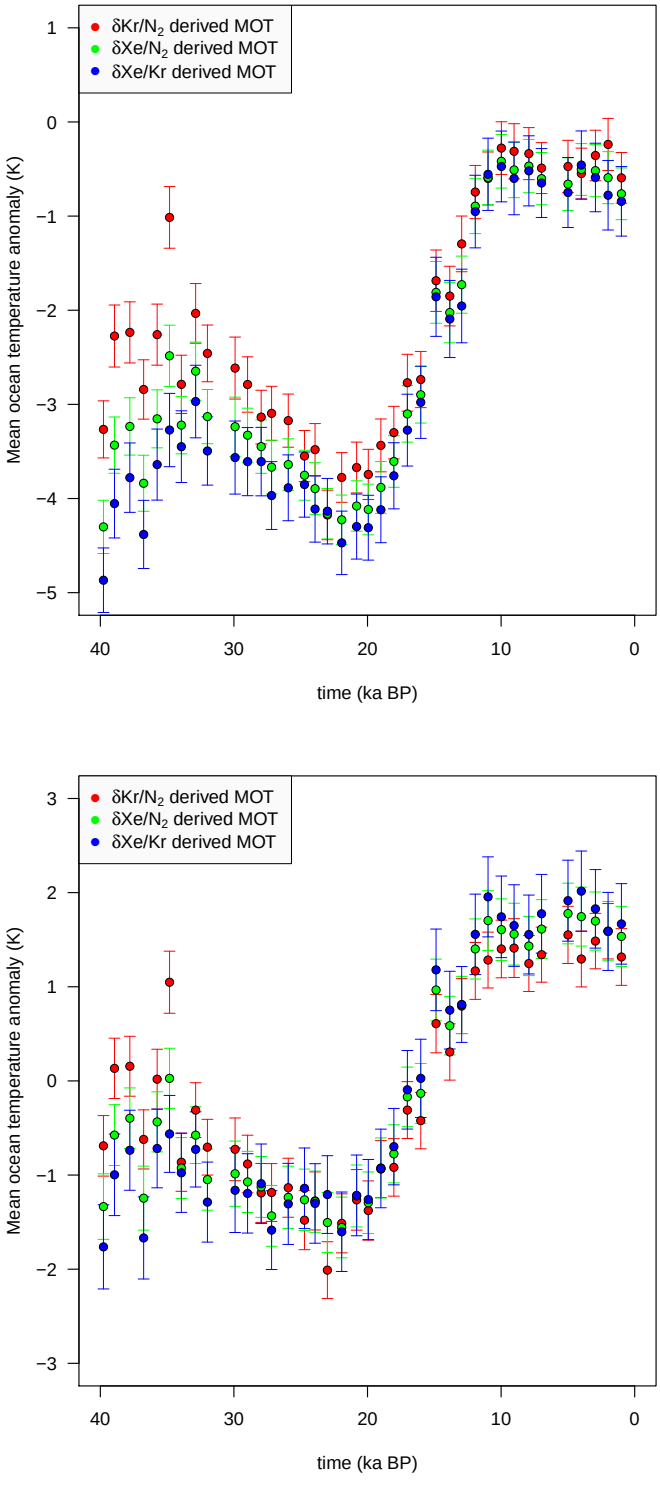

Fig. S5. MOT reconstructions from the EDC ice core for the individual elemental ratios $\delta Kr/N_2$, $\delta Xe/N_2$ and $\delta Xe/Kr$. (top) without HID correction, (bottom) with HID correction. The discrepancy between the three records increases with depth in the clathrated ice zone, suggesting that it might be due to fractionation from gas loss.

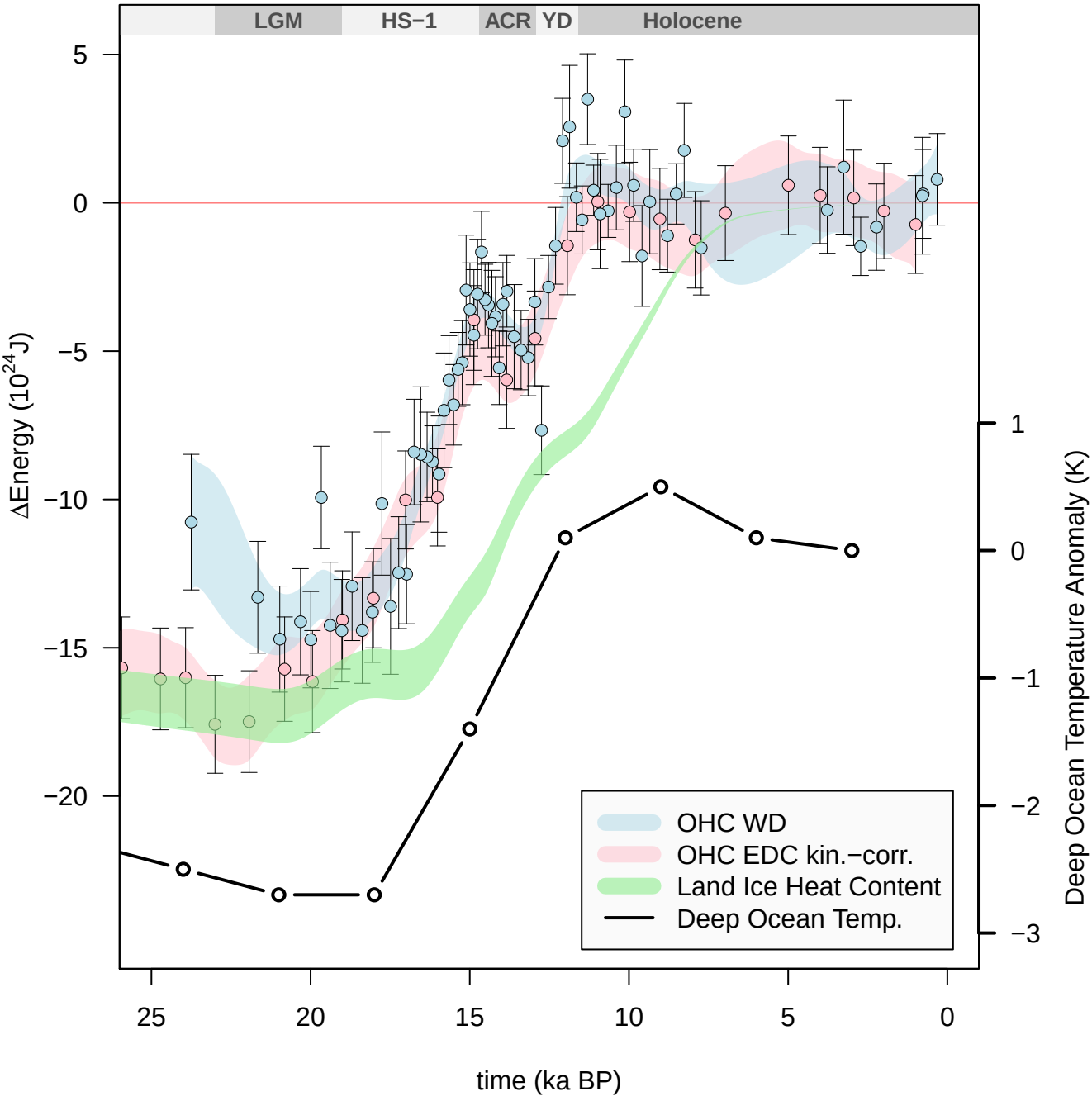

Fig. S6. Same as Figure 1, but with HID correction. A 3pt moving average HID fit is used to keep the additional noise introduced by the correction to a minimum.

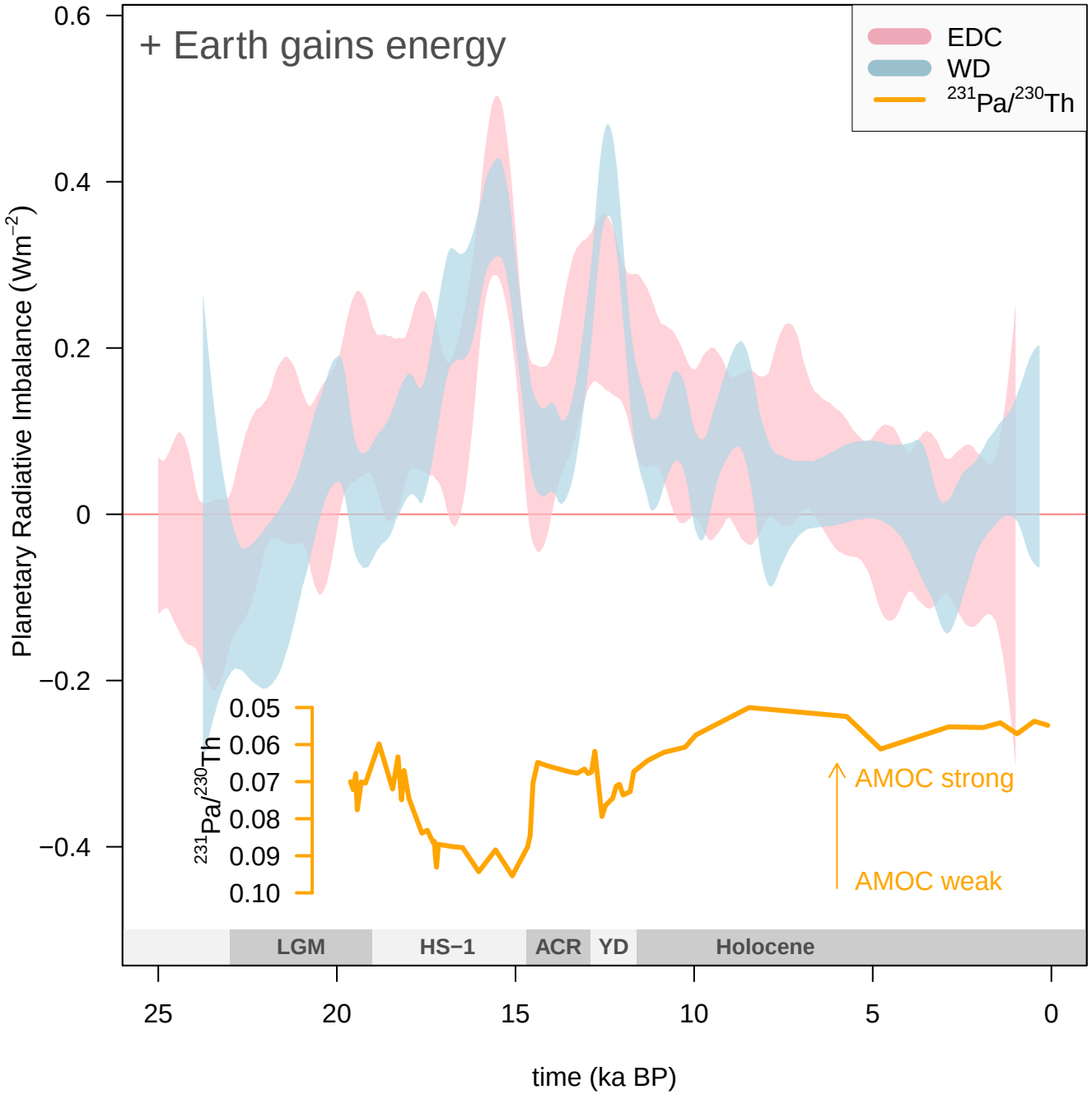

Fig. S7. Same as Figure 2, but with HID correction. A 3pt moving average HID fit is used to keep the additional noise introduced by the correction to a minimum.

References

1. Trenberth KE, Smith L (2005) The mass of the atmosphere: A constraint on global analyses. *Journal of Climate* 18(6):864–875.
2. Shakun JD, et al. (2012) Global warming preceded by increasing carbon dioxide concentrations during the last deglaciation. *Nature* 484(7392):49–54.
3. Boos WR (2012) Thermodynamic scaling of the hydrological cycle of the Last Glacial Maximum. *Journal of Climate* 25(3):992–1006.
4. Otto-Bliesner BL, et al. (2006) Last Glacial Maximum and Holocene climate in CCSM3. *Journal of Climate* 19(11):2526–2544.
5. Beltrami H, Smerdon JE, Pollack HN, Huang S (2002) Continental heat gain in the global climate system. *Geophysical Research Letters* 29(8):8–1–8–3.
6. Huang S (2006) 1851-2004 annual heat budget of the continental landmasses. *Geophysical Research Letters* 33(4).
7. Penrod EB, Elliott JM, Brown WK (1960) Soil temperature variation (1952–1956) at Lexington, Kentucky. *Soil Science* 90(5):275–283.
8. Andújar Márquez JM, Martínez Bohórquez MA, Gómez Melgar S (2016) Ground thermal diffusivity calculation by direct soil temperature measurement. application to very low enthalpy geothermal energy systems. *Sensors (Basel, Switzerland)* 16(26938534):306–306.
9. Gleeson T, Befus KM, Jasechko S, Luijendijk E, Cardenas MB (2015) The global volume and distribution of modern groundwater. *Nature Geoscience* 9:161.
10. Mohan C, Western AW, Wei Y, Saft M (2018) Predicting groundwater recharge for varying land cover and climate conditions – a global meta-study. *Hydrology and Earth System Sciences* 22(5):2689–2703.
11. Döll P, Fiedler K (2008) Global-scale modeling of groundwater recharge. *Hydrology and Earth System Sciences* 12(3):863–885.
12. Bethke CM, Johnson TM (2008) Groundwater age and groundwater age dating. *Annual Review of Earth and Planetary Sciences* 36(1):121–152.
13. Bassham JA, Lambers H (2018) *Encyclopædia Britannica Online*. (Encyclopædia Britannica, inc.).
14. Jeltsch-Thömmes A, Battaglia G, Cartapanis O, Jaccard SL, Joos F (2019) Low terrestrial carbon storage at the Last Glacial Maximum: constraints from multi-proxy data. *Climate of the Past* 15(2):849–879.
15. Schwander J, Stauffer B, Sigg A (1988) Air mixing in firn and the age of the air at pore close-off. *Annals of Glaciology* 10:141–145.
16. Buizert C, Severinghaus JP (2016) Dispersion in deep polar firn driven by synoptic-scale surface pressure variability. *The Cryosphere* 10(5):2099–2111.
17. Birner B, Buizert C, Wagner TJW, Severinghaus JP (2018) The influence of layering and barometric pumping on firn air transport in a 2-D model. *The Cryosphere* 12(6):2021–2037.
18. Kawamura K, et al. (2013) Kinetic fractionation of gases by deep air convection in polar firn. *Atmospheric Chemistry and Physics* 13(21):11141–11155.
19. Bereiter B, Shackleton S, Baggenstos D, Kawamura K, Severinghaus J (2018) Mean global ocean temperatures during the last glacial transition. *Nature* 553:39–44.
20. Baggenstos D (2015) Taylor Glacier as an archive of ancient ice for large- volume samples : Chronology, gases, dust, and climate. *PhD Thesis (UC San Diego)*.
21. Severinghaus JP, Grachev A, Battle M (2001) Thermal fractionation of air in polar firn by seasonal temperature gradients. *Geochem. Geophys. Geosyst.* 2(7).